Simulation of Deployment of a Flexible Solar Array

Oskar Wallrapp[*] and Simon Wiedemann[**]

[*]*Fachhochschule München – University of Applied Sciences, D-80335 Munich, Germany*
[**]*Cranfield University, College of Aeronautics, Cranfield, UK*

Abstract. The deployment of a solar array is simulated using the multibody program SIMPACK. The analyses are performed for 500 real-time seconds, which contain the three deployment phases, (I) jump-out, (II) steering phase and (III) deployed phase. The goal of the simulations is to check the influence of the flexibility of the solar array on the solar generator motions during these three phases against results obtained by a rigid body model simulation.

The modelling of flexible bodies is based on the widely used method of floating frame of reference formulation applying global shape functions (Ritz method). The preparation of a proper set of shape functions to represent the flexibility of the yoke and the six solar panels is one of the main objectives of this paper. For each of the components, eigenmodes and static modes for various boundary conditions are computed using the finite element program NASTRAN.

For a good convergence of the Ritz approximation with a small number of shape functions, the shape functions are selected using participation factors, that are computed for various load cases prior to the time simulations. The load cases are obtained, for example, by a rigid body simulation of the deployment phases. The proposed method of shape function selection using participation factors is demonstrated by examples.

1. Introduction

The deployment of a solar array as shown in Fig. 1 is one of the critical moments for a satellite structure. Therefore, simulations are performed to gain knowledge about the various structural loads during deployment. The model presented here consists of the central body of the satellite, along with a yoke and six panels, which are connected by revolute joints and deployment mechanisms. The central body is inertially fixed.

The deployment is undertaken in three phases:

I   In phase one – called *jump-out* – the completely folded solar panels are freed from their fixations, and then deployment springs drive the solar generator open against the
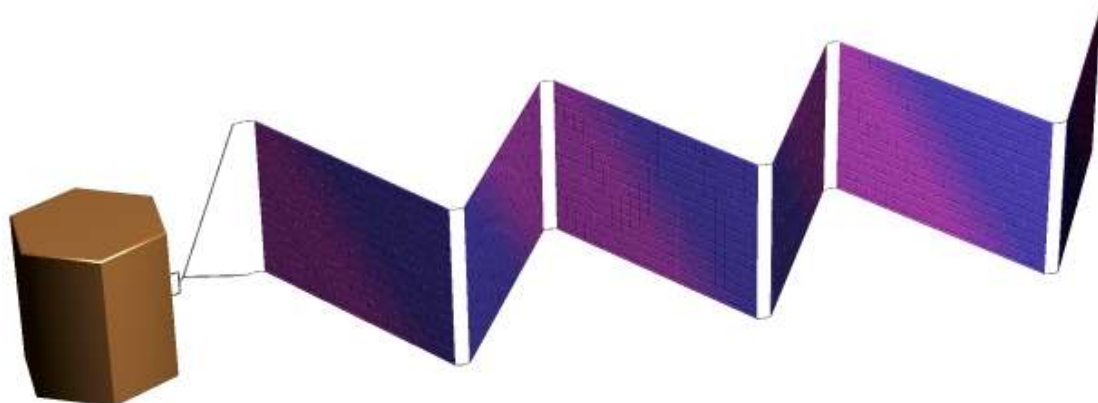

Figure 1 Scheme of the solar array of a satellite with the central body, the yoke and the six panels.

flexible cable mechanisms between the bodies. After some oscillations damped by various friction, a static equilibrium configuration of all the bodies and mechanisms is reached. This phase lasts 250 seconds.

II In following *steering phase*, a motor gear unit controls the further deployment until all panels and the yoke lay within one plane and get locked in this position. This phase lasts 110 seconds.

III In the locked and plane configuration the solar array performs a damped oscillation – *deployed phase*. The three phases take 500 real-time seconds in all.

In addition to the fast rigid body simulation, a simulation with a flexible yoke and panels is presented. The simulations are performed using the multibody program SIMPACK, which is based on an O(n) formalism and the floating frame of reference formulation [9]. As a consequence, the motion of a flexible body is a reference motion with superimposed small deformations using the Ritz method. The mode shapes and their corresponding mode shape matrices are pre-computed from results of a finite element analysis of the flexible body and are converted to the so-called standard input data (SID) [18]. The pre-processor FEMBS [19] calculates the SID for various FEM programs; the SID may also be imported by various MBS programs other than SIMPACK.

A known difficulty using the Ritz approach is the choice of proper mode shapes. The paper discusses the selection of mode shapes for various boundary conditions; the specific reference frames are referred to as Buckens frames, rigidly attached nodal frames and three-point body fixed frames. Normal vibration modes and mode shapes due to static loads (static modes) are used.

In order to reduce the computational burden and to increase the convergence of the simulation results, an efficient mode selection method is required, as is often stated in the literature. Refs. [2, 14, 15] discuss mode selection for multibody simulation in particular. Here, participation factors are used that are computed for various quasi-static load cases prior to time simulations.

The paper is organised as follows: Section 2 gives a brief description of the equations of motion. In section 3, the modelling of the rigid and flexible solar array is presented. Section 4 discusses the mode selection and computation of participation factors and section 5 shows the results of the simulations. The conclusion is given in section 6.

2. Brief Description of Equations of Motion

A multibody system is an assembly of bodies, joints, force elements and a global reference frame with respect to which a body moves. The global reference frame is inertially fixed or accelerated. The bodies are rigid or flexible and represent the inertia of the system. Joints and force elements are massless and are attached to nodes on the surface of the bodies. They cause forces and torques at the nodes and additionally, joints yield kinematical constraint equations [8, 11].

The equations of motion of a multibody system are efficiently derived by multibody formalisms that are based on data which describe the system elements and topology. Here, the Lagrangian equations of type one are discussed They are written as n_z redundant variables of position and velocity – $n_z \times 1$-matrices $\mathbf{z}_I$ and $\mathbf{z}_{II}$ – of the n bodies and the n_c constraint forces – $n_c \times 1$-matrix $\boldsymbol{\lambda}$ – of the n_G joints. The equations of motion in the so-called *descriptor form* with the dimension $2 n_z + n_c$ are given as [3]

$$\left. \begin{aligned} \dot{\mathbf{z}}_I &= \mathbf{Z}\, \mathbf{z}_{II} \\ \mathbf{M}\, \dot{\mathbf{z}}_{II} - \mathbf{G}^T \boldsymbol{\lambda} &= \mathbf{h}_a \\ \mathbf{g} &= 0 \quad \text{or} \quad \mathbf{G}\mathbf{z}_{II} = \boldsymbol{\kappa} \end{aligned} \right\} \quad \text{with} \quad \mathbf{G} = \frac{\partial \mathbf{g}}{\partial \mathbf{z}_I} \mathbf{Z} \tag{1}$$

where $\mathbf{Z} = \mathbf{Z}(\mathbf{z}_I)$ is the matrix of kinematic equations, $\mathbf{M} = \mathbf{M}(\mathbf{z}_I)$ is the mass matrix, $\mathbf{h}_a = \mathbf{h}_a(\mathbf{z}_I, \mathbf{z}_{II}, t)$ is the matrix of generalized applied forces due to stresses, gravity, body

and surface forces and torques, $\mathbf{g} = \mathbf{g}(\mathbf{z}_I, t)$ is the $n_c \times 1$-matrix of the implicit position constraint equations and $\mathbf{G} = \mathbf{G}(\mathbf{z}_I, t)$ is the $n_c \times n_z$-constraint matrix, the Jacobian of $\mathbf{g}$. Matrix $\boldsymbol{\kappa} = \boldsymbol{\kappa}(t)$ defines functions of time at joints. The matrices in (1) are the sum of matrices that describe a single body and its forces and torques (index i) and a single joint (index s). Thus

$$\left.\begin{array}{llll}
\mathbf{z}_I = \left[\mathbf{z}_I^i\right], & \mathbf{z}_{II} = \left[\mathbf{z}_{II}^i\right], & \boldsymbol{\lambda} = \left[\boldsymbol{\lambda}^s\right], & \mathbf{g} = \left[\mathbf{g}^s\right], \\
\mathbf{Z} = \mathrm{diag}\left[\mathbf{Z}^i\right], & \mathbf{M} = \mathrm{diag}\left[\mathbf{M}^i\right], & \mathbf{h}_a = \left[\mathbf{h}_a^i\right], \\
n_z = \sum_{i=1}^{n} n_z^i, & n_c = \sum_{s=1}^{n_G} n_c^s,
\end{array}\right\} \quad \text{where} \quad \begin{array}{l} i = 1, \cdots, n, \\ s = 1, \cdots, n_G. \end{array} \tag{2}$$

SIMPACK uses a topology that forms a multibody system with a tree structure and applies Eq. (1) for joints, leading to kinematically closed loops. More details are given in [9].

2.1 Kinematics of a Flexible Body

The model of a flexible body i is a continuum in general with internal constraints in particular such as beams and plates or a finite element model. Assuming that the deformations are small, a common formulation is that of a floating body reference frame $\{O^i, \underline{\mathbf{e}}^i\}$ and linearised equations of deformation [10]. The total motion is a (large) motion of the reference frame with respect to the global frame $\{O^I, \underline{\mathbf{e}}^I\}$ and small deformations with respect to the reference frame. O^I and O^i denote the origin, $\underline{\mathbf{e}}^I$ and $\underline{\mathbf{e}}^i$ the Cartesian basis of the coordinate frames. It is noted that all vectors in Fig. 2 and in the following figures are represented by coordinates with respect to the basis $\underline{\mathbf{e}}^i$.

The rotation of the body reference frame is given by $\boldsymbol{\alpha}^i(t)$ and $\boldsymbol{\omega}^i(t)$, the translation by $\boldsymbol{\rho}^i(t)$ and $\mathbf{v}^i(t)$, thus yielding the location and velocity of the body with respect to the global frame, see Fig. 2. The corresponding kinematical equations are

$$\begin{array}{l}
\underline{\mathbf{e}}^i = \mathbf{A}^i \, \underline{\mathbf{e}}^I \quad \text{where} \quad \mathbf{A}^i = \mathbf{A}^i(\boldsymbol{\alpha}^i), \\[2mm]
\tilde{\boldsymbol{\omega}}^i = \mathbf{A}^i \, \dot{\mathbf{A}}^{iT} \quad \text{or} \quad \dot{\boldsymbol{\alpha}}^i = \mathbf{Z}_r^i \, \boldsymbol{\omega}^i, \qquad \dot{\boldsymbol{\rho}}^i = \mathbf{v}^i + \tilde{\boldsymbol{\rho}}^i \, \boldsymbol{\omega}^i,
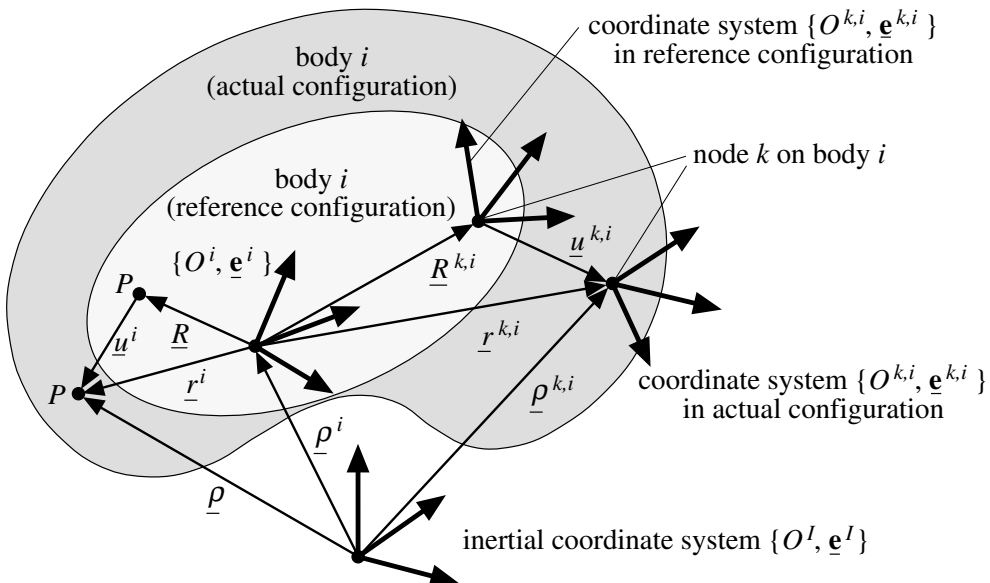\end{array} \tag{3}$$

Figure 2 General model of a representative body i.

where $\mathbf{Z}_r^i$ is a 3×3-matrix, relating the angular velocity coordinates $\boldsymbol{\omega}^i$ with the time derivatives of the angles $\boldsymbol{\alpha}^i$. In the reference configuration the position of all material points P with respect to the reference frame is given by $\mathbf{R}$. Models with internal constraints such as beams use rigid parts of the body that rotate. Their orientation is defined introducing a frame $\{P, \underline{\mathbf{e}}\}$ at P and is measured by the rotation matrix $\boldsymbol{\Gamma}^i = \boldsymbol{\Gamma}^i(\mathbf{R})$ satisfying $\underline{\mathbf{e}} = \boldsymbol{\Gamma}^i \underline{\mathbf{e}}^i$. In the reference configuration matrix $\boldsymbol{\Gamma}^i$ is mostly given by an identity matrix $\mathbf{E}$. In the actual configuration, the points P are inertially described by position $\boldsymbol{\rho}(\mathbf{R},t)$ and orientation $\mathbf{A}(\mathbf{R},t)$. The velocities are $\mathbf{v}(\mathbf{R},t)$ and $\boldsymbol{\omega}(\mathbf{R},t)$ for translation and rotation, respectively.

As shown in Fig. 2, vectors $\mathbf{u}^i(\mathbf{R},t)$ and $\boldsymbol{\vartheta}^i(\mathbf{R},t)$ are introduced for translational and rotational deformation, respectively. Thus

$$
\boldsymbol{\rho} = \boldsymbol{\rho}^i + \mathbf{r}^i, \qquad \mathbf{r}^i = \mathbf{R} + \mathbf{u}^i, \qquad \mathbf{v} = \mathbf{v}^i + \dot{\mathbf{r}}^i + \tilde{\boldsymbol{\omega}}^i \, \mathbf{r}^i, \qquad \dot{\mathbf{r}}^i = \dot{\mathbf{u}}^i,
$$
$$
\underline{\mathbf{e}} = \mathbf{A} \, \underline{\mathbf{e}}^I, \qquad \mathbf{A} \stackrel{lin}{=} \left(\mathbf{E} - \tilde{\boldsymbol{\vartheta}}^i \right) \boldsymbol{\Gamma}^i \, \mathbf{A}^i(\boldsymbol{\alpha}^i), \qquad\qquad \boldsymbol{\omega} \stackrel{lin}{=} \boldsymbol{\omega}^i + \dot{\boldsymbol{\vartheta}}^i. \tag{4}
$$

For $\mathbf{u}^i(\mathbf{R},t)$ and $\boldsymbol{\vartheta}^i(\mathbf{R},t)$, a Ritz approximation

$$
\left. \begin{aligned}
\mathbf{u}^i(\mathbf{R},t) &= \boldsymbol{\Phi}^i(\mathbf{R}) \, \mathbf{q}^i(t), \qquad \boldsymbol{\Phi}^i = \left[\Phi_{\alpha l}^i \right] \\
\boldsymbol{\vartheta}^i(\mathbf{R},t) &= \boldsymbol{\Psi}^i(\mathbf{R}) \, \mathbf{q}^i(t), \qquad \boldsymbol{\Psi}^i = \left[\Psi_{\alpha l}^i \right]
\end{aligned} \right\}, \quad \mathbf{q}^i(t) = \left[q_l^i(t) \right], \quad \begin{aligned} l &= 1, 2, \ldots n_q^i, \\ \alpha &\mathrel{\hat{=}} x, y, z, \end{aligned} \tag{5}
$$

is used where $\boldsymbol{\Phi}^i(\mathbf{R})$ and $\boldsymbol{\Psi}^i(\mathbf{R})$ are shape functions (mode shapes) and $\mathbf{q}^i(t)$ unknown time functions. n_q^i is the number of shape functions. Therefore, the variables in (2) to represent position and velocity of a body i and its kinematic matrix are

$$
\mathbf{z}_I^i = \begin{bmatrix} \boldsymbol{\rho}^i \\ \boldsymbol{\alpha}^i \\ \mathbf{q}^i \end{bmatrix}, \qquad \mathbf{z}_{II}^i = \begin{bmatrix} \mathbf{v}^i \\ \boldsymbol{\omega}^i \\ \dot{\mathbf{q}}^i \end{bmatrix}, \qquad \mathbf{Z}^i = \begin{bmatrix} \mathbf{E} & \tilde{\boldsymbol{\rho}}^i & \mathbf{0} \\ \mathbf{0} & \mathbf{Z}_r^i & \mathbf{0} \\ \mathbf{0} & \mathbf{0} & \mathbf{E} \end{bmatrix}, \tag{6}
$$

where $n_z^i = 6 + n_q^i$ is the number of position variables of body i. Substituting $\mathbf{R}$ by $\mathbf{R}^{k,i}$, Eqs. (4) and (5) describe the motion of a single node k of body i and its frame $\{O^{k,i}, \underline{\mathbf{e}}^{k,i}\}$ as shown in Fig. 2.

2.2 Conditions of Shape Functions and Constraints

Convergence of the Ritz method in (5) towards the solution of the partial differential equation describing body deformation is assured if the shape functions form a complete set of functions and if they satisfy the geometrical boundary conditions, [1]. Such functions are called *admissible functions*, [6]. The expansion theorem defines the conditions, under which *eigenfunctions* or *eigenmodes* form a complete set of admissible functions. Using eigenfunctions violating the dynamical boundary conditions, the convergence of the Ritz method is often poor, especially when evaluating the internal forces of a flexible body. Convergence can be improved significantly by introducing an expanded class of admissible functions, called *quasi-comparison functions*, [4, 5]. These are functions that fulfil dynamical boundary conditions, (at least a linear combination of these functions). In practice, the use of shape functions for static load cases (*static modes*) increase the convergence considerably in addition to eigenmodes.

The variables $\mathbf{z}_I$, $\mathbf{z}_{II}$ are not independent. Three types of constraints are considered:

a) The constraints of a specific model describe the internal body motions, e.g. the motion of rigid cross sections for the Bernoulli beam.

b) In (4) twelve variables $\boldsymbol{\rho}^i(t), \boldsymbol{\alpha}^i(t), \mathbf{u}^i(\mathbf{R},t)$ and $\boldsymbol{\vartheta}^i(\mathbf{R},t)$ define the motion of the coordinate frame $\{P, \underline{\mathbf{e}}\}$. Therefore six constraints are still required to compute the position and orientation of the body reference frame.

c) Joints between nodes of the bodies and of the global frame lead to constraint equations depending on $\mathbf{z}_I$ and time t.

By considering the selected shape functions $\boldsymbol{\Phi}^i(\mathbf{R})$ and $\boldsymbol{\Psi}^i(\mathbf{R})$ of a flexible body introduced in (5), the constraints of type a) are satisfied automatically. For the constraints defined in b) the following body reference frames are frequently used:

i) *Tangent* or node fixed frame at node $\mathbf{R} = \mathbf{R}^{Fi}$ yields $O^i = P(\mathbf{R} = \mathbf{R}^{Fi})$ and $\underline{e}^i \equiv \underline{e}(\mathbf{R} = \mathbf{R}^{Fi})$ and thus applying (5)

$$\mathbf{u}^i(\mathbf{R}^{Fi},t) = \boldsymbol{\Phi}^i(\mathbf{R}^{Fi})\,\mathbf{q}^i(t) = 0 \quad \text{and} \quad \boldsymbol{\vartheta}^i(\mathbf{R}^{Fi},t) = \boldsymbol{\Psi}^i(\mathbf{R}^{Fi})\,\mathbf{q}^i(t) = 0. \tag{7}$$

ii) Frame, which is based on three body nodes $\mathbf{R}^{Fi}$, $\mathbf{R}^2$ and $\mathbf{R}^3$ and so-called *chord* frame. The origin is given by $O^i = P(\mathbf{R} = \mathbf{R}^{Fi})$, the basis $\underline{e}^i$ is oriented on the planes expressed by the three nodes. This yields the following six conditions

$$\mathbf{u}^i(\mathbf{R}^1,t) = \boldsymbol{\Phi}^i(\mathbf{R}^{Fi})\,\mathbf{q}^i(t) = \mathbf{0}, \quad u_2^i(\mathbf{R}^2,t) = \boldsymbol{\Phi}_{2*}^i(\mathbf{R}^2)\,\mathbf{q}^i(t) = 0,$$

$$u_3^i(\mathbf{R}^2,t) = \boldsymbol{\Phi}_{3*}^i(\mathbf{R}^2)\,\mathbf{q}^i(t) = 0, \quad u_3^i(\mathbf{R}^3,t) = \boldsymbol{\Phi}_{3*}^i(\mathbf{R}^3)\,\mathbf{q}^i(t) = 0. \tag{8}$$

iii) *Tisserand* or mean-axis frame at the center of mass CM^i of the deformed body and its basis $\underline{e}^i$ rotates so that the relative angular momentum $\mathbf{H}_{rel}^i = \mathbf{0}$. In addition to $\mathbf{R}_{CM}^i = \mathbf{0}$ these definitions imply that the relative linear momentum $\mathbf{J}_{rel}^i = \mathbf{0}$. $\mathbf{J}_{rel}^i$ and $\mathbf{H}_{rel}^i$ are given by

$$\mathbf{J}_{rel}^i = \int_{V_0^i} \dot{\mathbf{u}}^i\,dm = \mathbf{C}_t^i\,\dot{\mathbf{q}}^i = \mathbf{0}, \quad \mathbf{H}_{rel}^i = \int_{V_0^i}\left(\tilde{\mathbf{R}}+\tilde{\mathbf{u}}\right)\dot{\mathbf{u}}^i dm = \left(\mathbf{C}_{r0}^i + \mathbf{C}_{r1}^i(\mathbf{q}^i)\right)\dot{\mathbf{q}}^i = \mathbf{0},$$

$$\text{and} \quad \mathbf{C}_t^i = \int_{V_0^i} \boldsymbol{\Phi}^i\,dm, \quad \mathbf{C}_{r0}^i = \int_{V_0^i} \tilde{\mathbf{R}}\,\boldsymbol{\Phi}^i dm, \quad \mathbf{C}_{r1}^i = \int_{V_0^i}\left(\boldsymbol{\Phi}^i\mathbf{q}^i\right)^{\widetilde{}}\boldsymbol{\Phi}^i dm. \tag{9}$$

In (9) V_0^i is the body volume and dm is the mass increment. A linearized form of (9), the *Buckens* frame, only takes into account matrix $\mathbf{C}_{r0}^i$.

The six constraint equations due to the reference frame given in (7) to (9) can be satisfied a priori by using corresponding boundary conditions for the shape functions. This is illustrated by the following examples: The mode shapes of a structure, which is clamped at node $\mathbf{R}^{Fi}$ satisfy (7) because $\boldsymbol{\Phi}^i(\mathbf{R}^{Fi}) = \mathbf{0}$ and $\boldsymbol{\Psi}^i(\mathbf{R}^{Fi}) = \mathbf{0}$. The chord frame is applied by using mode shapes of a simple supported beam of the length ℓ^i, where $\boldsymbol{\Phi}^i(\mathbf{R}^{Fi}) = \mathbf{0}$ and $\boldsymbol{\Phi}_{2*}^i(R_1^2 = \ell^i) = 0$. The Buckens frame is applied if mode shapes of an unsupported structure are used without the rigid body modes, because the integrals in (9) yield zero matrices for $\mathbf{C}_t^i$ and $\mathbf{C}_{r0}^i$. If in addition $\mathbf{C}_{r1}^i = \mathbf{0}$, a Tisserand frame is obtained. Using such a specific body reference frame, the mode shapes must be transformed accordingly to satisfy the geometrical boundary conditions, [12], prior to insertion into the equations of motion.

The last type of constraints is related to joints and leads to restricted motions of the two connected nodes with respect to each other. Assuming that a joint s is defined from node l of body j to node k of body i the relative position and orientation are given by

$$\underline{d}^s = \underline{\rho}^{k,i} - \underline{\rho}^{l,j} = \underline{e}^{k,i}\, \mathbf{d}^s, \quad \mathbf{B}^s = \mathbf{B}^s(\boldsymbol{\beta}^s) = \mathbf{A}^{k,i}\, \mathbf{A}^{l,j^T} \quad \text{for} \quad \underline{e}^{k,i} = \mathbf{B}^s\, \underline{e}^{l,j}. \tag{10}$$

The relative motion given by the matrices $\mathbf{d}^s = \left[d_\alpha^s\right]$ and $\boldsymbol{\beta}^s = \left[\beta_\alpha^s\right]$ can be expressed by (4) to (6) in terms of the system variables $\mathbf{z}_I$, and in case of excitations also in terms of time t. A joint s restricts $0 \le n_c^s \le 6$ motions of the relative variables $\mathbf{d}^s$ and $\boldsymbol{\beta}^s$ and their time derivatives and may be written in accordance with (2) as

$$\mathbf{g}^s(\mathbf{z}_I, t) = \mathbf{0} \quad \text{and} \quad \mathbf{G}^s(\mathbf{z}_I, t)\, \mathbf{z}_{II} = \boldsymbol{\kappa}(t). \tag{11}$$

Eq. (11) defines holonomical constraint equations for the variables describing the body reference motion and the deformation, [8].

2.3 Dynamics of a Flexible Body

Referring to the assumptions of the flexible body model as defined before, inertia forces, stresses, volume forces $\mathbf{k}_0^i(\mathbf{R}, t)$ due to gravity, surface forces $\overline{\mathbf{p}}_0^i(\mathbf{R}, t)$, forces $\mathbf{F}^{k,i}$, torques $\mathbf{L}^{k,i}$ due to force elements (subscript f), and joints (subscript c) at nodes k, i are considered.

The virtual power of these forces acting on n bodies in terms of the generalised velocities $\mathbf{z}_{II}^i$ as defined in (2) is

$$\delta P = \sum_{i=1}^n \delta \mathbf{z}_{II}^{i}{}^T \left(\mathbf{M}^i\, \dot{\mathbf{z}}_{II}^i - \mathbf{h}_a^i - \mathbf{h}_c^i\right) \quad \text{with} \quad \mathbf{h}_a^i = \mathbf{h}_\omega^i + \mathbf{h}_g^i + \mathbf{h}_e^i + \mathbf{h}_p^i + \mathbf{h}_f^i. \tag{12}$$

In (12) matrix $\delta \mathbf{z}_{II}^i$ denotes the virtual velocity of $\mathbf{z}_{II}^i$ and $\mathbf{M}^i$, $\mathbf{h}_a^i$ and $\mathbf{h}_c^i$ denote the corresponding generalised masses, applied forces and constraint forces. As shown in (12) matrix $\mathbf{h}_a^i$ is the sum of generalized applied forces such as the inertia forces $\mathbf{h}_\omega^i$ due to the angular velocity $\boldsymbol{\omega}^i$ in (3), the gravitational forces $\mathbf{h}_g^i$ due to $\mathbf{k}_0^i(\mathbf{R}, t)$, the internal forces $\mathbf{h}_e^i$ due to body deformations, the surface forces $\mathbf{h}_p^i$ due to $\overline{\mathbf{p}}_0^i(\mathbf{R}, t)$ and forces $\mathbf{h}_f^i$ arising from the nodal forces $\mathbf{F}_f^{k,i}$ and torques $\mathbf{L}_f^{k,i}$ due to force elements. Similarly, $\mathbf{h}_c^i$ is given by nodal forces $\mathbf{F}_c^{k,i}$ and torques $\mathbf{L}_c^{k,i}$ due to joints. Since $\delta \mathbf{z}_{II}^i$ depends on constraints of type c) given in (11), matrix $\mathbf{h}_c^i$ can be expressed in terms of the constraint matrix $\mathbf{G}^s$ and the Lagrange multipliers or constraint forces $\boldsymbol{\lambda}^s$. With (14) the equations of motion given in (1) and (2) are derived.

Now the matrices $\mathbf{M}^i$, $\mathbf{h}_e^i$, and $\mathbf{h}_f^i = \sum \mathbf{h}_n^{k,i}$ of all applied nodal forces and torques acting on body i are considered in detail. Partitioning these matrices in the same way as matrix $\mathbf{z}_{II}^i$ in (6) yields, [11, 18]

$$\mathbf{M}^i = \begin{bmatrix} m^i\, \mathbf{E} & & sym. \\ m^i\, \tilde{\mathbf{c}}^i & \mathbf{I}^i & \\ \mathbf{C}_t^i & \mathbf{C}_r^i & \mathbf{M}_e^i \end{bmatrix}, \quad \mathbf{h}_e^i = \begin{bmatrix} \mathbf{0} \\ \mathbf{0} \\ -\left(\mathbf{K}_e^i + \mathbf{K}_{geo}^i\right)\mathbf{q}^i - \mathbf{D}_e^i\, \dot{\mathbf{q}}^i \end{bmatrix}, \quad \mathbf{h}_n^{k,i} = \begin{bmatrix} \mathbf{F}^{k,i} \\ \tilde{\mathbf{r}}^{k,i}\, \mathbf{F}^{k,i} + \mathbf{L}^{k,i} \\ \boldsymbol{\Phi}^{k,i^T}\, \mathbf{F}^{k,i} + \boldsymbol{\Psi}^{k,i^T}\, \mathbf{L}^{k,i} \end{bmatrix} \tag{13}$$

Indices t, r and e denote the translation and rotation of the reference motion and the elastic deformation, respectively. Symbol m^i in (13) denotes the mass of body i. $\mathbf{I}^i$ and $\mathbf{c}^i$ are the inertia matrix and the position matrix of the center of mass CM^i of the deformed body with respect to the origin O^i. Sub-matrix $\mathbf{M}_e^i$ contains the generalised masses corresponding to the velocities $\dot{\mathbf{q}}^i$, while $\mathbf{C}_t^i$ and $\mathbf{C}_r^i$ are matrices representing coupling effects between reference motion and deformation they are already defined in (9). $\mathbf{K}_e^i$ is the generalized linear stiffness matrix of deformation and $\mathbf{K}_{geo}^i$ takes geometrical non-linearities due to large forces into account. $\mathbf{D}_e^i$ represents damping of the structure. Matrix $\mathbf{h}_n^{k,i}$ denotes the result of generalized nodal forces and torques at node k,i, where $\mathbf{r}^{k,i}$ is the position vector of the node defined in (4) if $\mathbf{R} = \mathbf{R}^{k,i}$. All the generalised forces and masses in (12) and (13) are algebraic expressions containing the variables (6) and integrals of the functions $\mathbf{\Phi}^i(\mathbf{R})$ and $\mathbf{\Psi}^i(\mathbf{R})$, [11, 18].

2.4 Multibody System Data

The equations of motion, as derived above, imply the definition of data to describe a multibody system. These data may be separated into data representing bodies, joints, force elements, the motion of the global reference frame and the system topology. All this is extensively discussed in the literature on dynamics of rigid body systems. In [7] an object oriented data model is proposed for such systems. It is extended by a set of standard input data describing flexible bodies in multibody systems, [18]. The definition of these data is based on equations (12) and (13), where the shape functions $\mathbf{\Phi}^i(\mathbf{R})$ and $\mathbf{\Psi}^i(\mathbf{R})$ are required.

As previously mentioned, eigenmodes and static modes of flexible body models, such as beams, plates and finite element structures provide a set of shape functions describing the deformation of the body approximately. The pre-processors BEAM [17] and FEMBS [19] have been developed to compute all input data of a flexible body i based on beam and finite element models respectively. Using structural data of a beam model, BEAM computes the eigenmodes and the standard data after mode selection. FEMBS inputs are mass, stiffness and mode shape matrices, as well as static modes of a finite element structure. The output are the standard data for a specific choice of modes. The flow of data is shown in Fig. 3. More details are given in [11].
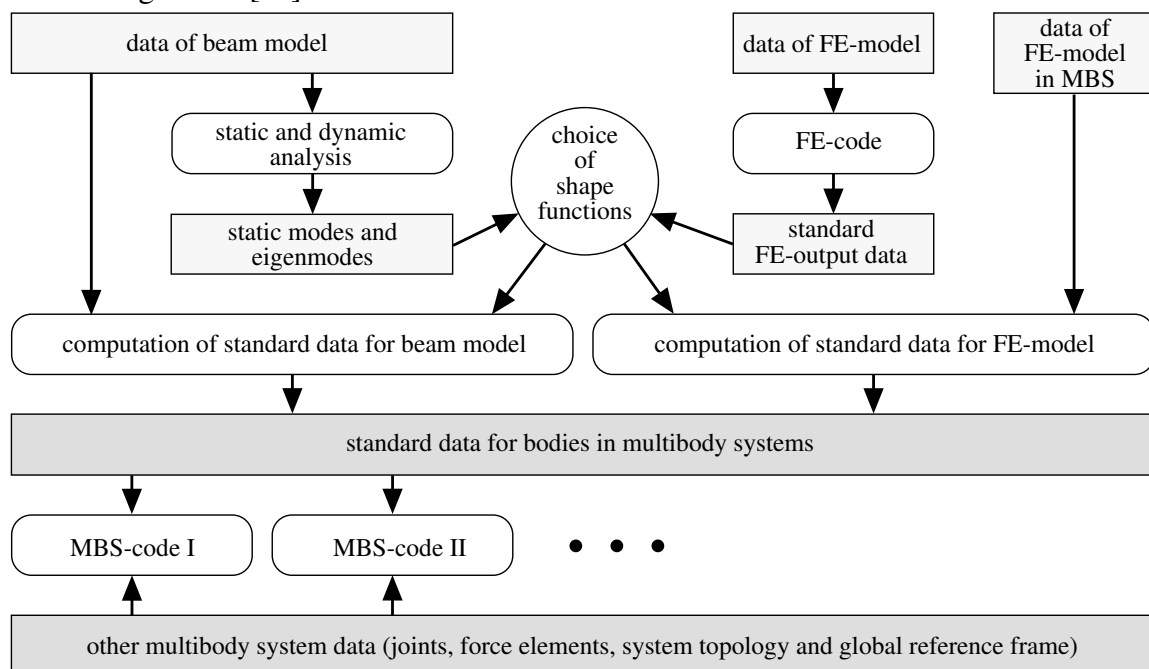

Figure 3 Multibody system data and pre-processors for computation of body data.

3. Modelling of the Satellite

3.1 Topology

The model consists of the central body, the yoke, and six panels. The central body is iner-tially fixed; while the yoke and panels are flexible bodies, attached to each other by two revolute joints (Fig. 1). Since SIMPACK differentiates between joints describing a tree topology and joints leading to kinematically closed loops, a test of the Gruebler condition is required. For the rigid yoke and panels, only the introduction of a rigid hinge body at each revolute joint and of the corresponding constraints between the hinge and the neighbour body (Fig. 4) leads to the desired $n_f = 7$ degrees of freedom (DOF's). The hinge bodies are connected to the yoke and panels respectively by revolute joints (type j1) at one side, leading to $n_c^s = 5$ constraints, and are connected to the other side by $n_c^s = 4$ constraints (joint type j2) or $n_c^s = 3$ constraints (joint type j3). Counting the number of all bodies n and all joints n_G as shown in Fig. 4 yields

$$n_f = 6\,n - \sum_{s=1}^{n_G} n_c^s = 7 \quad \text{for} \quad \begin{cases} n = 21, \\ n_G = 28, \end{cases} \quad n_c^s = \begin{cases} 5 \text{ for type j1 } (d_x^s = d_y^s = d_z^s = \beta_y^s = \beta_z^s = 0) \\ 4 \text{ for type j2 } (d_x^s = d_y^s = d_z^s = \beta_x^s = 0) \\ 3 \text{ for type j3 } (d_y^s = d_z^s = \beta_x^s = 0). \end{cases} \quad (14)$$

In the case of flexible bodies, the number of DOF's is given by seven plus the sum of the number of shape functions n_q^i of each body.

In the SIMPACK model, a joint of type j4 with six DOF's is introduced to describe the motion of the yoke and panels with respect to the base body. The hinges and their joints j1 are components of the tree structure. Finally, the joints j2 and j3 cause closed loop constraints. The number of DOF's of the tree structure $\hat{n}_z$ and of implicit constraints n_c are

$$\hat{n}_z = 7 \cdot 6 + 14 \cdot 1 + \sum_{i=1}^{n} n_q^i = 56 + \sum_{i=1}^{n} n_q^i, \qquad n_c = 7 \cdot (4 + 3) = 49. \quad (15)$$

This kind of topology allows for variation of the type of body reference frame as mentioned in section 2.2. Alternatively to the closed loop constraints, flexible spatial coupling elements with high stiffness can be used.
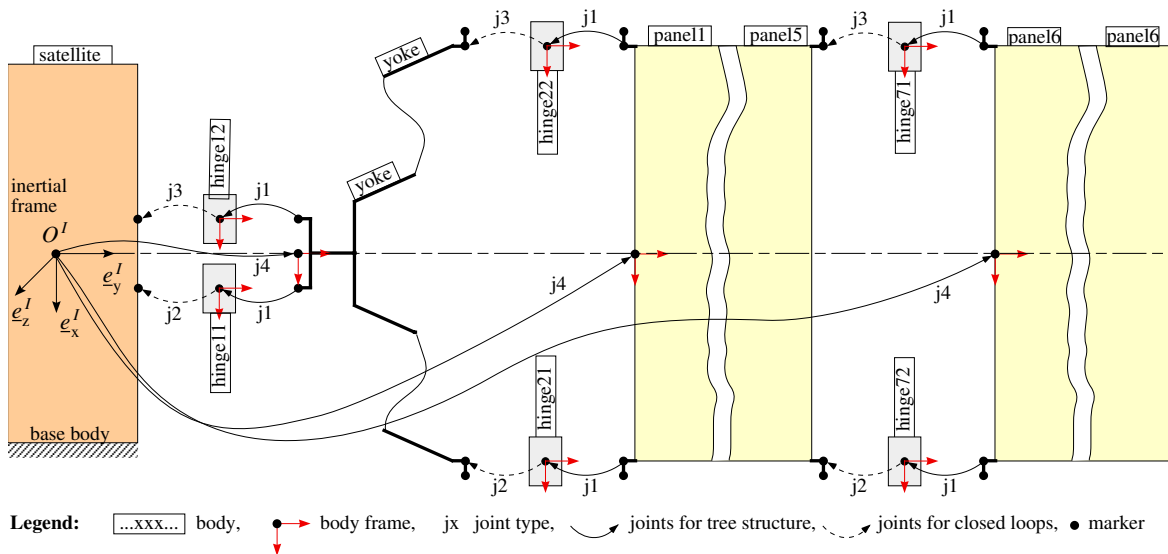

Figure 4 Topology of the solar array showing the tree structure and the closed loops.

3.2 Models of the Yoke and Panels

Basically, the yoke and panels are modelled using the finite element code NASTRAN (Fig. 5). The yoke and the six identical panels are represented by thin beam and plate structures. The yoke is 2.432 m long, while the panels are 3.610 m long, and the corresponding masses are 6.66 kg and 21.95 kg, respectively. Since FEMBS is restricted with respect to the DOF's of a single body, a nodal reduction to 69 nodes is applied to the panels.

The creation of standard body data for (1), (2), and (13) requires the definition of the reference frame and its corresponding boundary conditions, the computation of mode shapes and the calculations in FEMBS. Three cases of reference frames are discussed for the yoke and the panel in the following:

1) Buckens frame for a free body, yielding $\mathbf{C}_t^i = \mathbf{C}_{r0}^i = \mathbf{0}$ in (9) and six rigid body modes;
2) Buckens frame for a yoke supported by spherical joints at nodes 172 and 173 (panels at nodes 915 and 574 or 366 and 246), yielding $\mathbf{C}_{r0}^i = \mathbf{0}$ in (9) and one rigid body mode;
3) chord frame for a yoke supported as defined in b) and constrained by $d_z^s = 0$ at node 72, see (8). The panels are supported in a similar way.

According to these boundary conditions, natural frequencies are computed as listed in Table 1. Additionally, five static modes for the yoke are prepared for loads at node 71 and node 72 and boundary conditions as given in case b), where the free rotation is locked at node 173. The loads are a force in x, y and z at node 71, a force in z and a torque in x at node 72.

3.3 Models of Deployment Mechanisms

During the deployment defined in section 1, different force elements control the motions of the various bodies, i.e. the yoke and panels. The deployment springs provide the energy to move the yoke and the panels; the lock mechanisms fix the bodies in the proper positions; while the closed cable loops (CCL) harmonise the movement of the yoke and panels. Finally, a motor gear unit controls the rotation of the yoke with respect to the central body by two CCLs, (the motor unit with the two CCLs is called the Motor-CCL). Fig. 6 shows the position of all the force elements that are subsequently described in detail.

Deployment springs are attached to every hinge. Every spring supports the deployment with a constant torque of 1 Nm. The springs work from the folded position, such that the yoke is driven away from the central body, panel1 from the yoke, panel2 from panel1 etc. Since joint friction is not modelled, the springs are also damped (factor D_D) to avoid steady oscillations of the solar generator. With $\dot{\beta}$ being the relative angular velocity of the corresponding joint, the torque L_D is thus given as

$$L_D = L_0 + D_D\,\dot{\beta}. \tag{16}$$

Lock mechanisms are positioned on every hinge, like the deployment springs. They are activated if angle β of a revolute joint is equal to the lock angle β_0 for the first time. Lock mechanisms are also damped (factor D_L). With the stiffness k_L the force law is

$$L_L = 0 \qquad\qquad \text{if mechanism is not active,}$$
$$L_L = \left(\beta - \beta_0\right) k_L + \dot{\beta}\, D_L \qquad \text{if mechanism is active.} \tag{17}$$
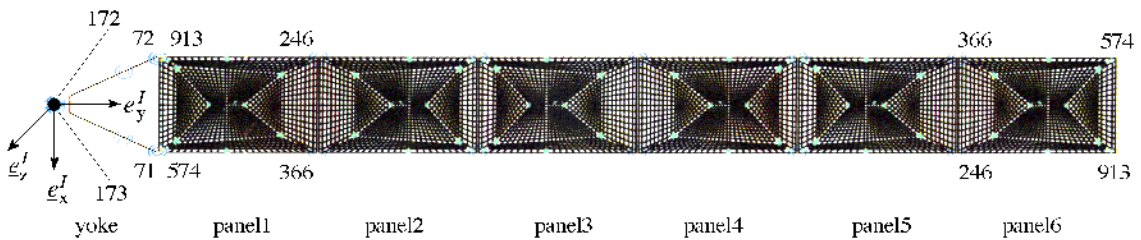
Figure 5 Finite element structure of the solar array including numbers of important nodes.

	Body ⇒	Yoke			Panel		
	Case ⇒	1)	2)	3)	1)	2)	3)
Mode and frequen. in Hz ⇒	1	B • 32.75	B • 3.584	B • 3.58	T • 3.97	T • 2.23	T • 2.23
	2	T • 33.23	T • 6.047	T • 4.05	B • 9.54	B • 6.77	B • 4.23
	3	• 36.66	• 15.921	• 14.26	• 14.13	•11.18	• 11.18
	4	• 44.63	• 37.502	• 31.99	• 21.71	• 17.90	• 11.52
	5	• 60.60	• 39.249	37.53	• 23.20	• 21.82	• 18.50
	6	• 72.37	• 39.840	39.84	27.96	• 27.88	23.11
	7	• 99.95	• 57.147	• 51.23	• 31.65	• 28.38	• 28.38
	8	• 110.58	• 63.098	63.09	• 33.13	29.31	• 29.01
	9	139.25	• 73.156	73.05	47.93	44.39	37.63
	10	157.04	• 107.56	• 96.86	48.93	44.55	44.55
	11	199.53	110.39	110.37	• 57.51	48.91	46.91
	12	• 207.67	140.24	• 138.63	62.69	• 54.84	• 54.84
	13	• 220.46	• 156.38	140.25	67.70	62.02	62.01
	14	279.83	215.31	• 191.48	76.65	67.13	62.42
	15	297.94	221.99	221.88	78.67	72.11	67.13
	16	319.67	277.87	• 242.63	79.16	77.60	74.96
	17	• 383.61	318.88	279.48	86.94	78.00	77.98
	18	389.10	• 381.77	• 331.63	105.95	80.42	80.42
	19	423.55	388.89	387.02	106.75	103.73	91.14
	20	520.55	423.28	390.58	109.02	105.10	105.06
	21	• 563.98	• 504.99	• 436.69	111.29	107.31	106.70
	22	577.76	534.08	508.96	114.67	108.75	108.54
	23	578.08	575.76	• 537.20	125.70	110.49	110.02
	24	• 607.04	577.51	575.91	140.12	123.45	120.68
	25	• 708.82	• 603.23	• 597.74	142.25	132.26	123.59
	26	739.74	611.15	605.46	150.52	133.97	132.26
	27	782.33	• 708.80	611.16	151.44	140.87	134.17
	28	• 869.67	740.25	• 732.43	169.96	143.80	143.76
	29	885.99	790.51	789.64	177.65	146.62	146.61
	30	921.12	869.48	• 866.65	180.54	153.38	149.35

Table 1 Natural vibration frequencies of the yoke and panel applying cases of reference frame:
1) = free structure, 2) = rotating structure and 3) = simple supported structure.
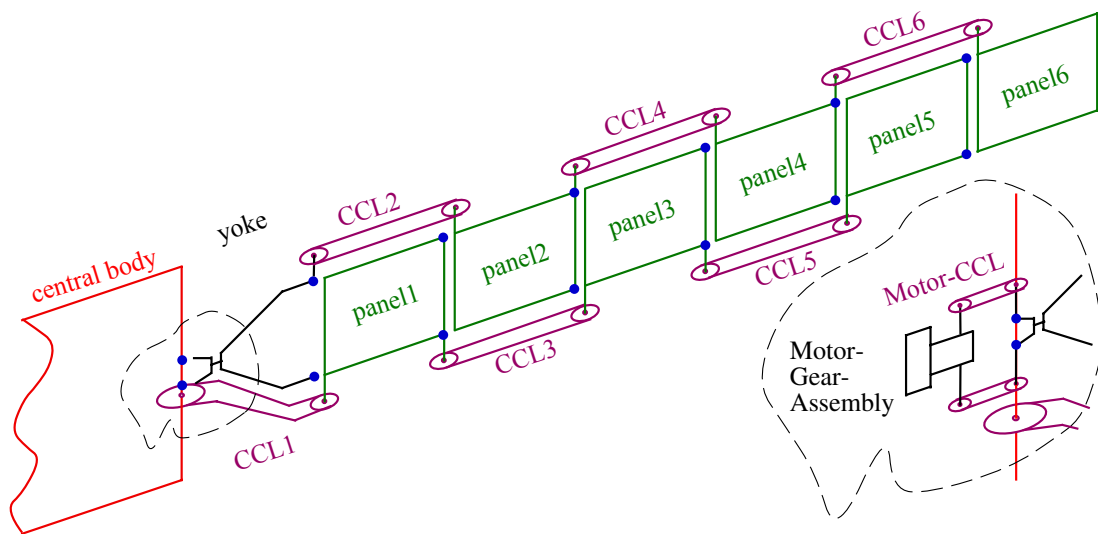The modes marked by • are taken for simulations in section 5. B denotes bending, T denotes torsion.

Figure 6 Position of the force elements representing the deployment mechanisms. Every • marks the position of a hinge with a revolute joint, a deployment spring and a lock mechanism.

Closed cable loops (CCL) connect the central body with panel1, the yoke with panel2, panel1 with panel3 etc., Fig. 6. Their function is to keep the linked bodies parallel to each other, except for CCL1. A CCL consists of two pulleys linked by a cable loop. If the two bodies linked by a CCL are not parallel, but distorted by an angle φ as shown in Fig. 7, the different cable forces produce a corrective torque L_C. Angle φ can be measured by marking both pulleys with lines M1 and M2, that are parallel in the initial configuration.

Since the cable forces are always parallel to an imaginary line connecting the two pulley centres, F_C always coincides with this imaginary line. With a cable stiffness k_C, a pre-tension F_0, the change of distance between the pulley centres $d - d_0$, pulley radius r and distortion angle φ the force laws are

$$\left. \begin{aligned} F_1 &= F_0 + (d - d_0)\, k_C + \varphi\, r\, k_C & \text{with} \quad F_1 \geq 0, \\ F_2 &= F_0 + (d - d_0)\, k_C - \varphi\, r\, k_C & \text{with} \quad F_2 \geq 0, \end{aligned} \right\} \Rightarrow \begin{cases} F_C = F_1 + F_2, \\ L_C = (F_1 - F_2)\, r. \end{cases} \tag{18}$$

F_1 and F_2 can-not be negative since they are caused by cables.

CCL1 is different to all other CCLs because of its relation of pulley radii: the radius of pulley1 is two times the radius of pulley2. Therefore, if the yoke rotates through an angle β with respect to the central body, panel1 rotates through 2β with respect to the yoke, see Fig. 8. If β is 90 degrees the yoke and panel1 lay within one plane. Whith regards to the other CCLs, if panel2, panel4 and panel6 are kept parallel to the yoke and panel3 and panel5 are kept parallel to panel1, then all the bodies lie within one plane. In this position, the lock mechanisms are activated and fix one body with its neighbours. As shown in Fig. 8 the force laws for pulley2 of CCL1 are

$$\left. \begin{aligned} F_1 &= F_0 + (d - d_0)\, k_C + \varphi\, r\, k_C & \text{with} \quad F_1 \geq 0, \\ F_2 &= F_0 + (d - d_0)\, k_C - \varphi\, r\, k_C & \text{with} \quad F_2 \geq 0, \end{aligned} \right\} \Rightarrow \begin{cases} F_{C1r} = (F_1 + F_2)\cos\xi, \\ F_{C1t} = (F_1 - F_2)\sin\xi, \\ L_{C1} = (F_1 - F_2)\, r. \end{cases} \tag{19}$$
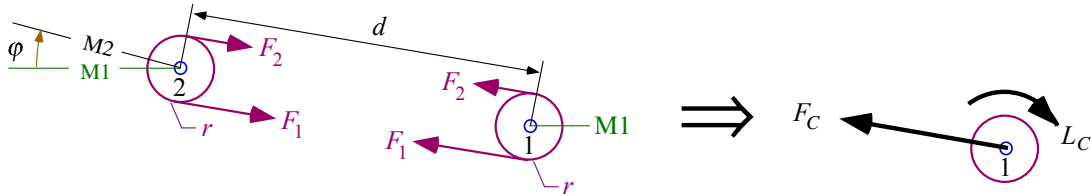

Figure 7 Cable forces F_1 and F_2 of CCL for distorted bodies leading to forces and torques F_C and L_C.
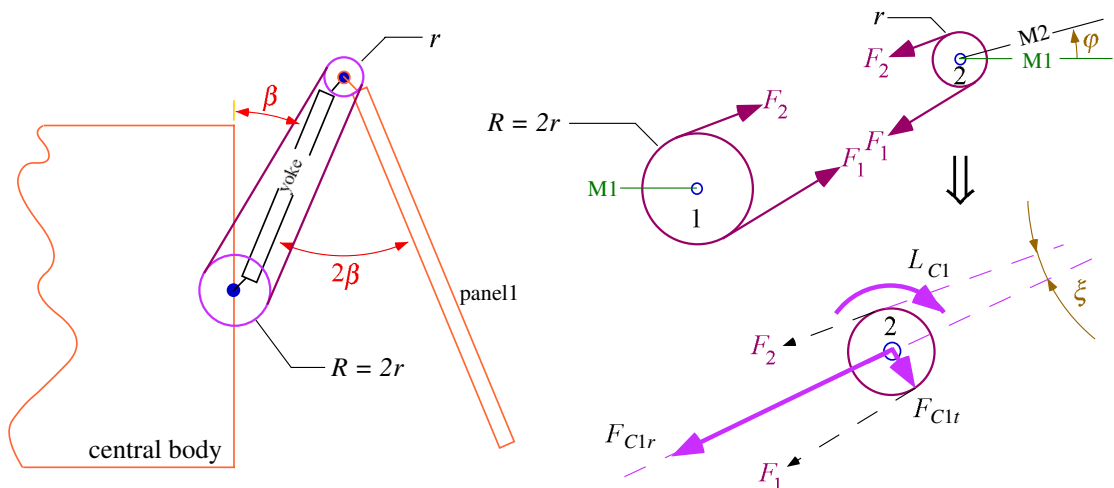

Figure 8 Forces and torques of CCL1 for distorted bodies

F_1 and F_2 lead to the radial and tangential forces F_{C1r} and F_{C1t} and the torque L_{C1}. Eqs (18) and (19) hold true for the following assumptions: First, the cable forces F_1 and F_2 acting on a pulley always lie within the plane of the pulley and second, two pulleys building one CCL are always parallel.

The Motor-CCL controls the rotation of the yoke with respect to the central body as shown in Fig. 6. Except for the cable elasticity, CCL1 to CCL6 avoid motions of panel1 to panel6 if the yoke rotation is locked. The Motor-CCL stands still at the beginning of the jump-out phase described in section 1. After the jump-out oscillations have calmed down, the Motor-CCL is activated and rotates the yoke slowly with respect to the central body until all the bodies appear within one plane and get locked; in this instant, the Motor-CCL is stopped. The force laws for each of the two cable loops of the Motor-CCL are equal to the force laws of the normal CCLs given in (18). With β being the angle between the yoke and central body, Ω the angular velocity of the motor, a relation of radii 1:1, t_M the time when the Motor-CCL starts working, t as the actual time, and t_0 as the initial time, the difference angle φ is given by

$$
\begin{aligned}
\varphi &= \beta - \beta(t_0) & &\text{if } t < t_M, \\
\varphi &= \Omega\left(t - t_M\right) + \left(\beta - \beta(t_0)\right) & &\text{if } t \geq t_M.
\end{aligned}
\tag{20}
$$

Eqs. (16) to (20) are active referring to the deployment phases defined in section 1.

4. Mode Selection Using Participation Factors

As mentioned in section 2, eigenmodes and static modes to increase the convergence of the Ritz approximation are used to describe body deformations of multibody systems. For the yoke and panels, 30 eigenmodes (without rigid body modes) for three kinds of reference frames, as defined in section 3, are prepared (Table 1). Static modes may be included additionally. Of all these mode shapes, a proper set with a reasonable number of shapes is selected for the yoke and the panels and is inserted into the equations of motion. Since the mode shapes are complex 3D shapes, a selection by hand based on the natural frequencies and their corresponding mode shapes is unlikely to be optimal. Therefore, the participation factor method is introduced.

4.1 Participation Factors

The deformation of a flexible body i with respect to the reference frame motion given by $\boldsymbol{\rho}^i$ and $\boldsymbol{\alpha}^i$ is described by displacements $\mathbf{u}^i(\mathbf{R}, t)$ and angles $\boldsymbol{\vartheta}^i(\mathbf{R}, t)$. They are written as a sum of known shape functions and functions $q_l^i(t)$, $l = 1, \dots n_q^i$, as shown in (4) and (5). Thus, the position and orientation of a nodal frame at node k on i with respect to the global frame are

$$
\boldsymbol{\rho}^{k,i} = \boldsymbol{\rho}^i + \mathbf{R}^{k,i} + \mathbf{u}^{k,i}(q_l^i), \qquad \mathbf{A}^{k,i} = \left(\mathbf{E} - \tilde{\boldsymbol{\vartheta}}^{k,i}(q_l^i)\right)\boldsymbol{\Gamma}^{k,i}\,\mathbf{A}^i(\boldsymbol{\alpha}^i),
$$

$$
\text{where } \mathbf{u}^{k,i} = \left[u_\alpha^{k,i}\right], \; u_\alpha^{k,i} = \sum_{l=1}^{n_q^i}\Phi_{\alpha l}^{k,i}\,q_l^i, \qquad \boldsymbol{\vartheta}^{k,i} = \left[\vartheta_\alpha^{k,i}\right], \; \vartheta_\alpha^{k,i} = \sum_{l=1}^{n_q^i}\Psi_{\alpha l}^{k,i}\,q_l^i.
\tag{21}
$$

If $\mathbf{u}^{k,i}$ and $\boldsymbol{\vartheta}^{k,i}$ are the correct solution (or an approximation), the share of q_l^i in the deformation is given as

$$
P_{ul} = \left|u_{\alpha l}^{k,i}\big/u_\alpha^{k,i}\right| = \left|\Phi_{\alpha l}^{k,i}\,q_l^i\big/u_\alpha^{k,i}\right| \qquad \text{and} \qquad P_{\vartheta l} = \left|\vartheta_{\alpha l}^{k,i}\big/\vartheta_\alpha^{k,i}\right| = \left|\Psi_{\alpha l}^{k,i}\,q_l^i\big/\vartheta_\alpha^{k,i}\right|.
\tag{22}
$$

Eq.(22) defines the so-called participation factors. Calculation of the quotient $P_{ql} = |q_l/q_{l\,\mathrm{max}}|$ is only allowed, if all shape functions are normalised (e.g. if the modal mass matrix $\mathbf{M}_e^i$ is an identity matrix).

For computation of (22), an estimation of q_l^i is proposed solving a quasi-static configuration of the body i due to a specific load case. The loads are estimated or obtained by a rigid body simulation. Assuming that $\mathbf{M}_e^i\,\ddot{\mathbf{q}}^i + \mathbf{D}_e^i\,\dot{\mathbf{q}}^i \ll \mathbf{K}_e^i\,\mathbf{q}^i$ and neglecting gyroscopical and geometrical stiffening terms, (12), (13) and (6) yields for body i

$$\mathbf{K}_e^i\,\mathbf{q}^i - \mathbf{G}_e^{i\,T}\,\boldsymbol{\lambda} = \underbrace{-\mathbf{C}_t^i\left(\dot{\mathbf{v}}^i + \tilde{\boldsymbol{\omega}}^i\,\mathbf{v}^i - \mathbf{g}^i\right) - \mathbf{C}_{r0}^i\,\dot{\boldsymbol{\omega}}^i - \mathbf{O}_{e0}^i\,\boldsymbol{\omega}_q^i}_{\text{inertia forces}} + \sum_k\left(\boldsymbol{\Phi}^{k,i\,T}\,\mathbf{F}^{k,i} + \boldsymbol{\Psi}^{k,i\,T}\,\mathbf{L}^{k,i}\right) \quad (23)$$

$$\mathbf{g}(\mathbf{z}_I(\mathbf{q}^i)) = \mathbf{0} \quad \text{and} \quad \mathbf{G}_e^i = \partial\mathbf{g}/\partial\mathbf{q}^i. \qquad (24)$$

In (23), $\mathbf{K}_e^i$ is the generalised stiffness matrix, $\mathbf{C}_t^i$ and $\mathbf{C}_{r0}^i$ are matrices given by (9), $\dot{\mathbf{v}}^i$, $\dot{\boldsymbol{\omega}}^i$, $\mathbf{v}^i$ and $\boldsymbol{\omega}^i$ are accelerations and velocities of the reference frame (3), $\mathbf{g}^i$ is the gravity, $\boldsymbol{\omega}_q^i$ is a 6×1 matrix of products of $\boldsymbol{\omega}^i$ and $\mathbf{O}_{e0}^i$ a matrix of mass integrals representing centrifugal forces [16]. The sum of these terms represents inertia forces. $\mathbf{F}^{k,i}$ and $\mathbf{L}^{k,i}$ are applied forces and torques at nodes k,i, which are summarised for all nodes k of body i. If the shape function $\boldsymbol{\Phi}^i$ and $\boldsymbol{\Psi}^i$ satisfy the kinematical conditions a priori, $\mathbf{g}$ in (24) is independent of $\mathbf{q}^i$, $\mathbf{G}_e^i$ equals zero and the static equilibrium Eq. (23) are independent of constraint forces $\boldsymbol{\lambda}$.

Defining $\dot{\mathbf{v}}^i$, $\dot{\boldsymbol{\omega}}^i$, $\mathbf{v}^i$, $\boldsymbol{\omega}_q^i$, $\mathbf{F}^{k,i}$, $\mathbf{L}^{k,i}$ and $\boldsymbol{\lambda}$ as given quasi-static loads, the variables $\mathbf{q}^i = [q_l^i]$ are obtained solving the linear equations (23), thus allowing for evaluation of the participation factors P_{ul}, $P_{\vartheta l}$ and P_{ql} in (22).

4.2 Examples of Simple Beam

The first example demonstrates the approximation of the deformation of a cantilever beam with a torque L^B at the tip (Fig. 9-a). The beam is modelled as a flexible body $i = 1$ with a tangent frame and natural modes of the cantilever beam (Fig. 9-b). From geometrical and material data, the matrices in (23), $\mathbf{K}_e^i$, $\mathbf{G}_e^i = 0$, $\boldsymbol{\Phi}^A$, $\boldsymbol{\Phi}^B$, $\boldsymbol{\Psi}^A$ and $\boldsymbol{\Psi}^B$ at nodes A and B are calculated, yielding $\mathbf{q}^i$ and the deformations at the tip given in $\mathbf{u}^{k,i}$ and $\boldsymbol{\vartheta}^{k,i}$. Here $\boldsymbol{\rho}^i$ and $\boldsymbol{\alpha}^i$ are zero. The participation factors for a configuration as given in Fig. 9-a) are plotted in Fig. 9-c). It shows that the share of the modes higher than four is smaller than 1 % in displacement y^B, but for the slope α^B, all modes are required to have an error of less than 1 %.

In a second example we consider a rotating beam in a quasi-static equilibrium with loads
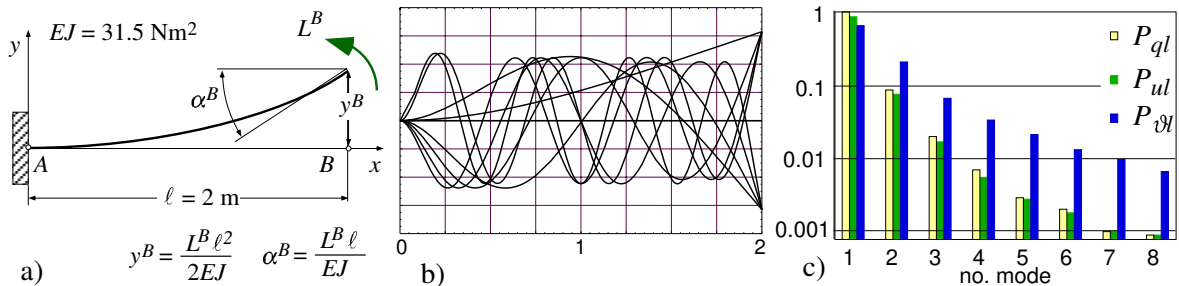

Figure 9 Participation factors of natural modes to approximate the static equilibrium of a cantilever beam
a) Static problem, b) mode shapes of cantilever beam, c) participation factors on solution of a)
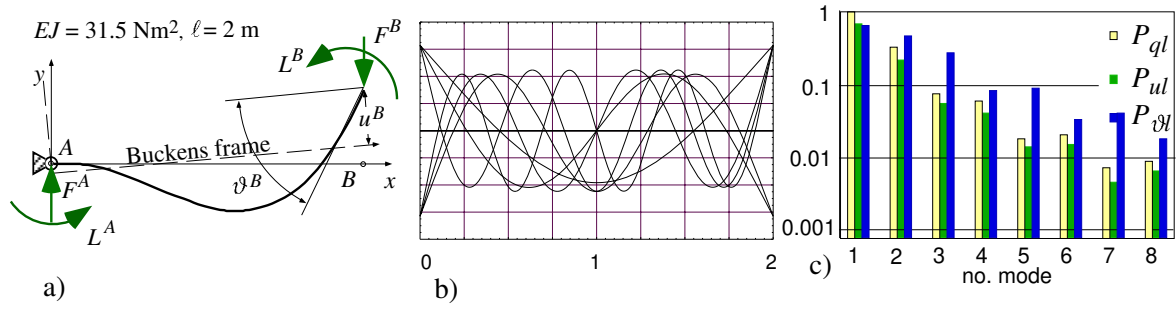
Figure 10 Participation factors of natural modes to approximate the static equilibrium of a rotating beam
a) Static problem, b) mode shapes of unsupported beam, c) participation factors on solution of a)

$F^B = -2$ N and $L^B = 3$Nm (Fig. 10-a). This problem is to be solved with a flexible body i attached to a revolute joint and using a Buckens frame with natural modes of an unsupported beam (Fig. 10-b). Inserting the given data into (23) and (22) yields participation factors as shown in Fig. 10-c). Here, the constraint forces $\boldsymbol{\lambda}$ at the hinge (point A) are taken into account, and $\boldsymbol{\rho}^i$ and $\boldsymbol{\alpha}^i$ are non-zero. As the participation factors in Fig. 10-c) prove, the deformation of the beam with respect to the body frame requires all eight modes achieving an error of less than 1 %. As in the previous example, the slope is more sensitive.

4.3 Participation Factors for the Yoke

The yoke is a flexible body supported by hinges at the satellite side (at nodes 172, 173) and the panel side (node 71, 72; see Fig. 5). As listed in Table 1, 30 natural modes for three kinds of reference frames are prepared. To select a reduced set of modes, the participation factor method for the frame case 2) – Buckens frame rotating at hinges at node 172, 173 with mode shapes of a rotating structure – is applied.

During the deployment of the solar array, the loads required in (23) are estimated using a rigid body model. Fig. 11 shows the nodal forces and torques at node 71 and 72. Taking the load cases at time $t = 50$ sec and $t = 290$ sec, from (22) and (23) we obtain the participation factors P_{ql} as well as P_{ul} and $P_{\vartheta l}$ for all nodes of interest. Fig. 12 shows P_{ql} and the influence on the deformation at nodes 71 and 72. Modes with factors smaller than 1 % are neglected. The remaining dominant mode shapes for the yoke are listed in (25). Fig. 12 shows that the eigenmodes do not converge continuously; modes 21 and 27 have a bigger share in the solution than the previous modes.

Mode shape numbers for the yoke: 1, 2, 3, 4, 5, 6, 7, 8, 9, 10, 13, 18, 21, 25, 27.   (25)

The computation of participation factors for other load cases and nodal displacements allows for the selection of a set of mode shapes that satisfy all the various load cases (i.e. selecting the mode shapes in a quasi-optimal fashion). Static modes can also be taken into account. In
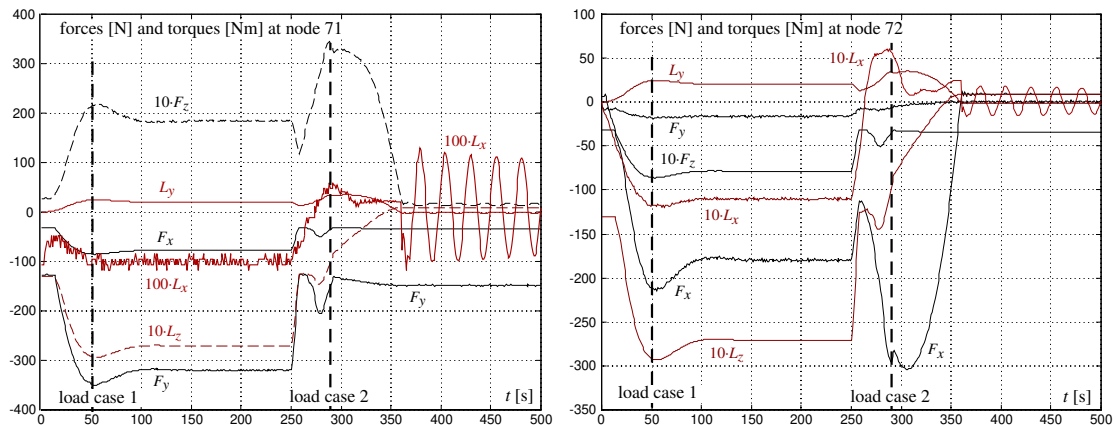

Figure 11 Results of the deployment of a solar array using the rigid body model.
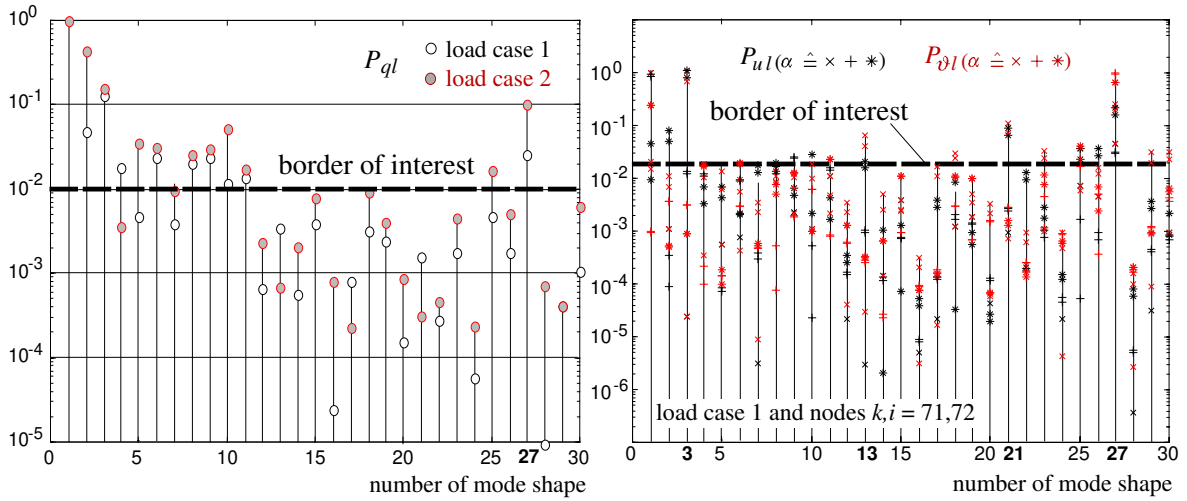
Figure 12 Participation factors for mode shapes of the rotating yoke structure.

a similar way, the shape functions of the panels are chosen and marked by • in Tab. 1.

5. Simulation Results of Deployment the Solar Array

Based on the descriptions of the bodies, joints and deployment mechanisms in section 3 and the mode selection in section 4, the deployment is simulated for various models of bodies [20]. Four models are discussed below:

I   All bodies are rigid, where $\hat{n}_z = 56$, see (15).

II The yoke and panels are flexible. The flexibility of the yoke is represented by 15 eigenmodes of mode set 2) – the rotating structure, see (25). For the panels, eight eigenmodes of mode set 2) are used, see Tab. 1. $\hat{n}_z$ equals 119.

III The yoke and panels are flexible as in II described by 15 and eight eigenmodes, respectively, but the modes are taken from unsupported structures – case 1), as given in Tab. 1.

IV As in II but the modes shapes of the yoke and the panels are obtained by the simple supported structures, see case 3) in Tab. 1.

The CPU time is 189 sec for the rigid model I, 4287 sec for model II and 4857 sec for model III. Fig. 13 shows the deployment of the solar array as defined in section 1. The deployment begins with the jump-out phase with the yoke and panels completely folded and
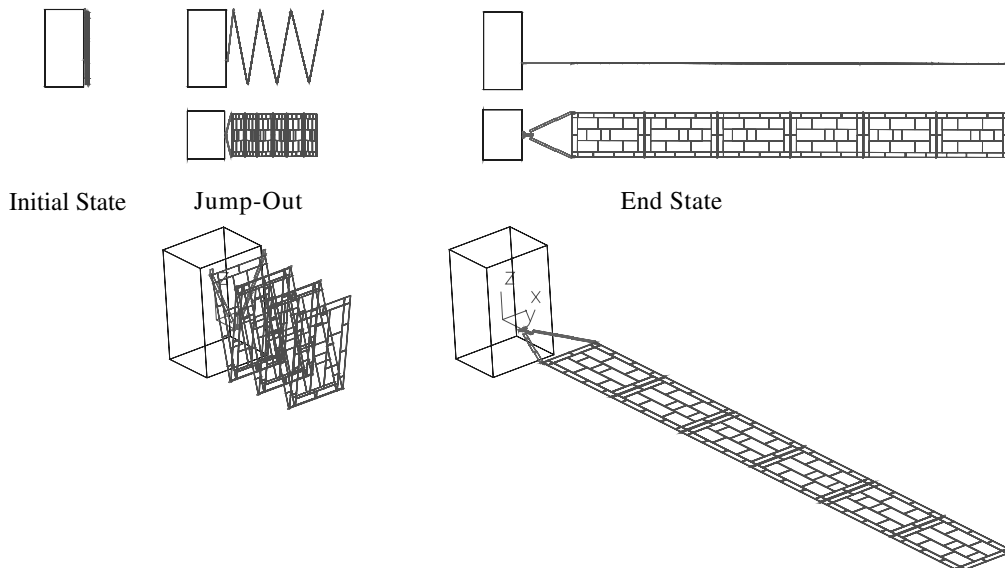

Figure 13 Motion of the solar array during the deployment.

lasts 250 sec. Then the Motor-CCL is activated and rotates the yoke as defined by (20) – steering phase. After about 360 sec, the panels are locked and the Motor-CCL is stopped. The deployed configuration is reached. For 140 sec or more, the panels keep oscillating with small amplitudes. The natural damping of the structure is assumed to be 2 %.

In Fig. 14, the torques of CCL1, CCL6, and of one of the Motor-CCLs are shown for the rigid model I and the flexible model II. At the end of the jump-out phase the corrective torque L_C of CCL6 is exactly –2 Nm caused by the two deployment springs at panel6. Since one CCL passes over its corrective torque L_C to the following via the bodies it connects, CCL1 has to compensate 12 Nm (= 6·2 Nm) at pulley2 and, due to the relation of the radii, 24 Nm at pulley1 (Fig. 8). The two Motor-CCLs have to compensate 12 Nm of CCL1, plus the torque resulting from F_{C1t} given in (19) times the length of the yoke plus 2 Nm of the yoke deployment springs. Since F_{C1t} times the length of the yoke is also exactly 12 Nm, each of the two Motor-CCLs has to compensate 13 Nm.

A comparison of models I and II shows that the torques decrease only about 2 % during the jump-out phase if the bodies are flexible, and 21 % during the steering phase. The oscillation in the deployed configuration is almost the same for both models. Differences between models I and II are small.

In Fig. 15 (left side) the absolute angles $\alpha_y^{k,i}$ and $\alpha_z^{k,i}$ at node k,i = 813 of panel6 are plotted. For model I, the angles are zero. In the flexible models, panel6 rotates about the y-
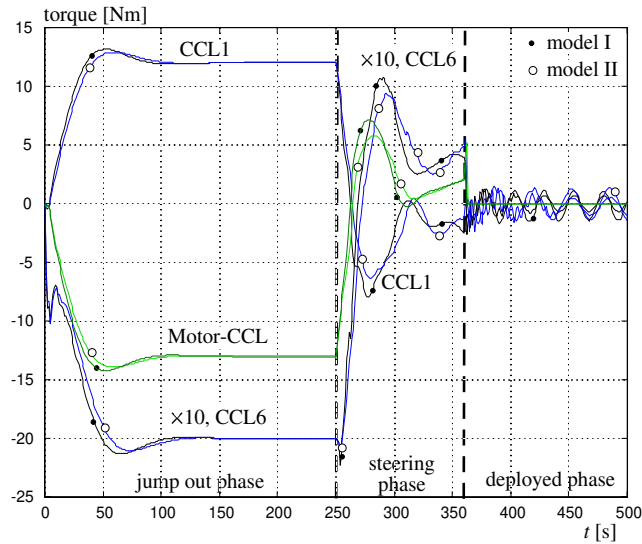

Figure 14 Results of time history of the deployment for the rigid model I and flexible model II.
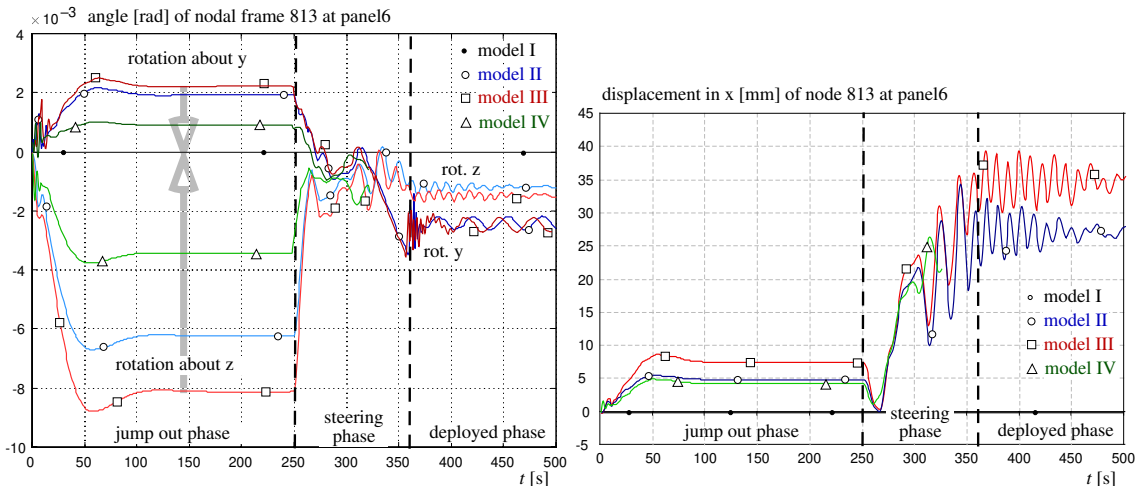

Figure 15 Results of time history of the deployment for the rigid model I and flexible models II, III, and IV.

and z-axis. In the deployed configuration, panel6 has a steady state value of $\alpha_y^{k,i} = 0.002$ rad that leads to displacements at node 574 and 913 (Fig. 5). Compared to the rigid model I, the elastic deviation in the z-direction is -2.7 mm and $+2.7$ mm at nodes 574 and 913, respectively.

Figure 15 (right side) shows the displacement in x-direction at node 813 of panel6. As mentioned before, the rigid body model provides no values, the flexible models result in about 30 mm steady state deformations after the deployment. Figure 15 proves that the differences between model II and III or IV are quite significant for rotations and a structure described by mode shapes with stiffer boundary conditions decreases the amplitudes.

Figure 16 (left side) shows the influence of the static modes on the results. The only difference between the models is one additional static mode for the yoke and for each of the panels. As can be seen, one additional static mode for each flexible body can change the results significantly, even if the number of mode shapes is relatively high.

Figure 16 (right side) illustrates the effect of increasing the number of mode shapes on the yoke from 15 up to 30 modes. The number of mode shapes for the panels is 8 in both models. It demonstrates the efficiency of a mode shape selection using the participation factor method: For 15 additional mode shapes (i.e. an increase of 100 % in the number of mode shapes) of the yoke, the results are slightly changed, although the flexibility of the yoke is the most dominant factor in the simulations.

In [20], more models are analysed for other sets of mode shapes and integrator settings and also for various static modes. The simulation results of those models are similar to the results presented here.
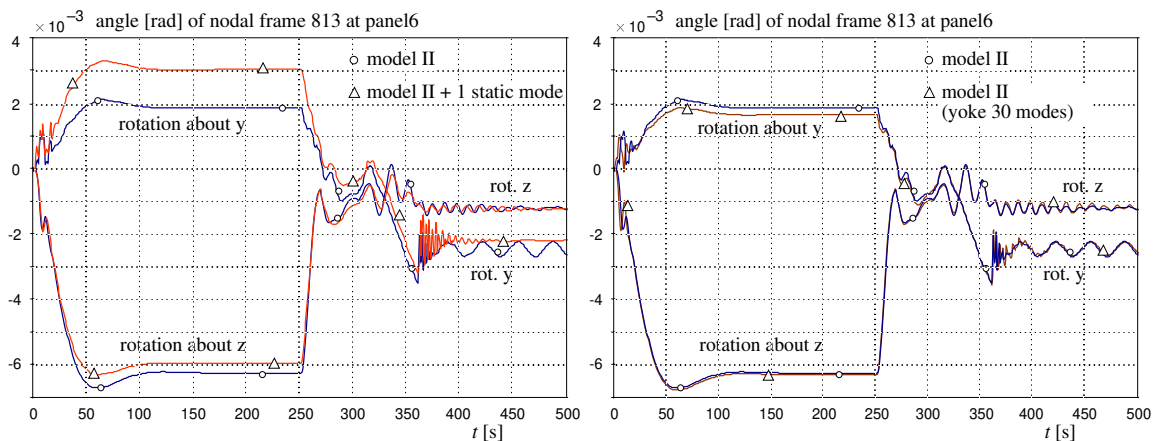

Figure 16 Results of time history of the deployment for variations numbers of mode shapes.

6. Conclusion

The deployment of a satellite solar array is simulated using the multibody program SIMPACK. A rigid body model I is compared with three flexible models II, III and IV, applying various sets of shape functions. The deployment mechanisms are implemented in detail for the three phases of deployment: jump-out phase, steering phase and deployed phase.

The flexibility of the yoke and panels is represented by a set of natural modes and some static modes obtained by a finite element analysis. In order to reduce the computational burden a participation factor method is applied to select the significant modes. The factors of each mode as shown in Fig. 12 are computed solving a quasi-static equilibrium of the flexible body, and the loads are obtained by a rigid body simulation. A simulation with the full set of modes (Fig. 16) demonstrates the power of the method.

The comparison of the results of the rigid body model I with the flexible body models II, III and IV shows that flexible bodies cause a slightly changed torque in the closed cable mechanisms. The steady state rotations and the deflection in x-direction of the panels are only occur for the flexible models, and the rotations about the y-axis are caused by deformations of the panels, whereas rotations about the z-axis are caused by the flexibility of the yoke. The solar generator is relatively stiff and the magnitudes of deformation are therefore relatively

small. The differences of the deformations between the flexible models II, III and IV are significant and need further research in the usage of the multibody program SIMPACK.

Acknowledgements

References

[1]   H. Bremer, F. Pfeiffer, *Elastische Mehrkörpersysteme*. Teubner Studienbücher, Mechanik, B. G. Teubner, Stuttgart, 1992.

[2]   S. Dietz, *Vibration and Fatigue Analysis of Vehicle Systems Using Component Modes*. Fortschr.-Berichte VDI, Reihe 12, Nr. 401, VDI-Verlag, Düsseldorf, 1999.

[3]   E. Eich-Soellner, C. Führer, *Numerical Methods in Multibody Dynamics*. Teubner-Verlag, Stuttgart, 1998.

[4]   P. Hagedorn, *The Rayleigh-Ritz Method With Quasi-Comparison Functions in Nonself-Adjoint Problems.* Journal of Vibration and Acoustics, 115, 1993, pp. 280-284.

[5]   L. Meirovitch, P. Hagedorn, *A New Approach to the Modelling of Distributed Non-Self-Adjoined Systems.* Journal of Sound and Vibration, 178(2), 1994, pp. 227-241.

[6]   L. Meirovitch, M. K. Kwak, *Convergence of the Classical Rayleigh-Ritz Method and the Finite Element Method.* AIAA Journal, 28(8), 1990, pp. 1509-1516.

[7]   M. Otter*, et al.*, *An Object Oriented Data Model for Multibody Systems,* in *Proc. Int. Symp. on Advanced Multibody System Dynamics,* (W. Schiehlen, ed.), Kluwer Acad. Publ., 1993, pp. 19-48.

[8]   R. E. Roberson, R. Schwertassek, *Dynamics of Multibody Systems*. Springer-Verlag, Berlin, 1988.

[9]   W. Rulka, *SIMPACK - A Computer Program for Simulations of Large-Motion Multibody Systems,* in *Multibody System Handbook,* (W. Schiehlen, ed.), Springer-Verlag, Berlin, 1990, pp. 265-284.

[10]   R. Schwertassek, *Flexible Bodies in Multibody Systems,* in *Computational Methods in Mechanical Systems,* (J. Angeles and E. Zakhariev, ed.), Springer-Verlag, Berlin, 1997, pp. 329-363.

[11]   R. Schwertassek, O. Wallrapp, *Dynamik flexibler Mehrkörpersysteme*. Vieweg Verlag, Braunschweig, 1999.

[12]   A. A. Shabana, *Resonance Conditions and Deformable Body Coordinate Systems.* J. Sound and Vibration, 192(1), 1996, pp. 389-398.

[13]   A. A. Shabana, *Flexible Multibody Dynamics: Review of Past and Recent Developments.* Multibody System Dynamics, 1, 1997, pp. 189-222.

[14]   J. T. Spanos, W. S. Tsuha, *Selection of Component Modes for Flexible Multibody Simulation.* Journal of Guidance, 14(2), 1991, pp. 278-286.

[15]   O. Verlinden, *Simulation du comportement dynamique de systemes multicorps flexibles comportant des membrures de forme complexe*, Faculte Polytechnique de Mons, Ph.-D.-Thesis, 1994.

[16]   O. Wallrapp, *Standard Input Data of Flexible Members for Multibody System Codes,* in *Advanced Multibody System Dynamics — Simulation and Software Tools,* (W. Schiehlen, ed.), Kluwer Academic Publishers, Dordrecht, 1993, pp. 445-450.

[17]   O. Wallrapp, *Beam — A Pre-Processor for Mode Shape Analysis of Straight Beam Structures and Generation of the SID File for MBS Codes, User's Manual*, Deutsche Forschungsanstalt für Luft- und Raumfahrt (DLR), Inst. Robotik und Systemdynamik, Oberpfaffenhofen, Report Version 3.0, March 1994.

[18]   O. Wallrapp, *Standardization of Flexible Body Modeling in Multibody System Codes, Part I: Definition of Standard Input Data.* Mechanics of Structures and Machines, 22(3), 1994, pp. 283-304.

[19]   O. Wallrapp, A. Eichberger, J. Gerl, *FEMBS - An Interface Between FEM Codes and MBS Codes, User Manual for ANSYS, NASTRAN, and ABAQUS*, INTEC GmbH, Wessling, Report Version 3.0, January 1997.

[20]   S. Wiedemann, *Entfaltanalyse Solargenerator unter Berücksichtigung von Elastizitäten mit SIMPACK*, Fachhochschule München - Univ. of Applied Sciences, Diplomarbeit, 1999.